CrystEngComm

Manipulation of Carrier Concentration, Crystallite Size and Density in Polycrystalline Anatase TiO2 via Amorphous-Phase Medium Range Atomic Order

Journal:	*CrystEngComm*
Manuscript ID:	CE-ART-01-2015-000048.R1
Article Type:	Paper
Date Submitted by the Author:	02-Feb-2015

Complete List of Authors:	Barlaz, David; University of Illinois, Chemical and Biomolecular Engineering Seebauer, Edmund; University of Illinois, Chemical & Biomolecular Engineering

SCHOLARONE™
Manuscripts

Manipulation of Carrier Concentration, Crystallite Size and Density in Polycrystalline Anatase TiO_2 via Amorphous-Phase Medium Range Atomic Order

D. Eitan Barlaz and Edmund G. Seebauer*

Department of Chemical and Biomolecular Engineering, University of Illinois, Urbana, Illinois 61801, USA

Abstract

Thin-film semiconducting anatase TiO_2 finds several applications, including photocatalysis, wherein control over carrier concentration and other material properties would be useful. The present work employs atomic layer deposition to fabricate thin amorphous films of TiO_2, which are then annealed into polycrystalline anatase. Variations in the temperature and growth rate for deposition, as well as in the ramp rate and final temperature employed during the annealing, propagate into changes in one or more of the final carrier concentration, crystallite size and bulk density. Many of these surprising findings can be interpreted in terms of medium range atomic order existing in the initial amorphous films, and demonstrate that the order can be manipulated and exploited to some degree.

* To whom all correspondence should be addressed. Electronic address: eseebaue@illinois.edu

Introduction

Thin-film semiconducting anatase TiO_2 finds applications in gas sensors[1] and photocatalysts for self-cleaning windows and other weather-exposed surfaces[2, 3], and for anti-microbial[4] and anti-fouling coatings[5]. For photocatalysts in particular, reaction rates would benefit greatly if minority photocarriers could be driven more efficiently to the surface[6] through the manipulation of internal electric fields. Such manipulation is commonplace in conventional optoelectronics via control of background carrier concentration, but conceptual translation to metal oxides has lagged considerably[7]. Control is difficult in metal oxides because of special challenges in carrier concentration metrology[8], the dearth of dopants having shallow donor or acceptor levels[9], the effects of poorly-controlled concentrations of native point defects serving as donors or acceptors[10, 11] and the dominant effects of charged defects at grain boundaries[9]. The need for defect engineering to resolve these issues is becoming increasingly recognized[12, 13], although most efforts for TiO_2 (for photocatalysts[14, 15] and memristors[16]) have focused on doping. To avoid the problems inherent in metal oxide doping, this laboratory and others have demonstrated that film thickness[9, 17] can control defects that influence carrier concentration, which propagates beneficially into rates of photocatalysis[18] and supported metal catalysis[19]. For practical applications, however, thickness and carrier concentration represent independent design variables that should remain decoupled. Other variables such as synthesis temperature[20, 21], growth rate[22], and annealing temperature[20, 23] have been employed reported for phenomenological control of morphology in anatase but these works have not linked the defect characteristics to carrier concentration.

The present work fills that gap in important ways by showing that synthesis variables other than doping can propagate into changes in carrier concentration. Thin films of anatase are fabricated in amorphous form by atomic layer deposition (ALD), and subsequently annealed to yield crystalline anatase. ALD was selected over other synthesis techniques for its ability to easily manipulate synthesis conditions & produce high purity films. Variations in the temperature and growth rate for depositing the amorphous films, as well as in the ramp rate and

final temperature employed during the post-growth annealing to anatase, often propagate into changes in carrier concentration of the final crystalline films or into the crystallite size or bulk density. These surprising findings are interpreted in terms of the existence of "medium range order" (MRO) in the initial amorphous films. Experimental evidence for MRO already exists for Si[24] and TiO_2[25], and computational evidence exists for metal oxides in general[26]. MRO represents a special type of atomic configuration within amorphous semiconductors wherein the atoms are arranged into topologically crystalline grains, roughly 1 nm in diameter, that are isolated and severely strained and therefore do not produce coherent diffraction or easily interpreted Raman peaks[27]. These grains can be conceptualized as subcritical nuclei for the growth of crystallites. Efforts to manipulate MRO are still embryonic even for Si, and have been limited to increasing the concentration of the MRO regions for use as crystalline seeds[28, 29]. The present work extends, by different methods and concepts, that work to TiO_2 – regarding both the production of MRO seeds and the manipulation of their growth into stable crystallites.

Experimental

The synthesis chamber was a 3 liter six-way cross with a Teflon (DuPont 852-202, 850-799) coating to prevent reactions with the chamber walls. The chamber was pumped to a base pressure of approximately 50 mTorr by a Varian SD200 direct drive pump with a nominal operating pressure of 200 mTorr monitored by a 10 Torr scale MKS Baratron capacitance manometer. The specimen platform was custom built to house a 150 W halogen bulb (Osram 24V GY6.35) for heating. A chromel-alumel (type K) thermocouple soldered to the platform (but not in direct contact with the specimens) monitors temperature.

Initially amorphous TiO_2 films were deposited as follows. Substrates for fashioned from Sb-doped Si(100) wafers (Silicon Quest International) with n-type resistivity of 0.013 Ω*cm. Wafers were cut into 4 cm^2 square substrates, which were then degreased by successive rinsing in acetone, isopropanol, and acetone before drying with compressed N_2. Subsequent etching in 48% HF (Sigma Aldrich) for 1 min and rinsing in deionized water for 1 min removed the native

oxide initially present. The deposition source gases TTIP (titanium tetraisopropoxide, Strem Chemicals Inc., 98%) and H_2O (DI, no further purification) were delivered in a carrier stream of 20 psi N_2 gas (SJ Smith, 99.999%). A flow rate of 60 SCCM was maintained by MKS 1179A mass flow controllers and an MKS 247D 4-Channel Readout. The TTIP bubbler was heated by a water bath to 60 °F, the water bubbler was allowed to stay at room temperature. Deposition temperatures ranged from 150 to 275°C. Growth rates were controlled by varying precursor pulse lengths while holding purge lengths static, and varied from 0.25 to 7.5 nm/cycle.

Thickness measurements of as-deposited films were obtained via ellipsometry using a Rudolph Technologies AutoEL II single wavelength instrument. The single wavelength ellipsometer provided a preliminary confirmation that the as-deposited films were amorphous, as index of refraction varies significantly with crystallinity and exhibits sample to sample variation[†] for polycrystalline material. X-ray diffraction (XRD) was performed on select films to further confirm that as-deposited films were amorphous.

The amorphous films were crystallized by annealing for 24 hr in a tube furnace (Barnstead Thermolyne F79300) under an ambient atmosphere. The annealing ramp rate and temperature were 20 °C/min and 550°C unless otherwise specified below. For ramp rates near 1000°C/s, a rapid thermal processing tool (Jipelec JETfirst) was used in line with a Lindberg/Tempress Model 8500 tube furnace, also under an ambient atmosphere. In this case, specimens were held at 550 °C for 5 minutes in the tool after ramping before rapid cooling back to room temperature. Following this cooling, samples were placed in the Lindberg tube furnace already at 550 °C for 24 hr. This two-step annealing process sought to replicate the 24 hr constant temperature annealing time for all the other specimens, given the severe tool-imposed constraints on annealing time.

Morphological characterization was accomplished by X-ray methods using a PANalytical X-ray diffractometer. The copper X-ray source operated at 45 kV and 40 mA. The detector was

[†] $n_{amorphous}$=2.05, $n_{polycrystalline}$=2.45 to 2.55

a PIXcel high speed line detector capable of single-strip count rates of 2.5×10^{6} s^{-1}. For X-ray reflectivity (XRR) scans, a 1/32 degree slit was used with the divergence slit; XRD scans used a 1/2 degree slit. XRR 2θ-ω scans were taken from 0.2° – 3° to encompass the critical reflection angle and easily discernable thickness fringes. XRD 2θ-ω scans were taken from 20° – 80° to encompass all easily discernable anatase peaks as well as possible major rutile peaks. Scans were fit to Powder Diffraction File (PDF) cards for anatase and rutile TiO_2[‡]. Detailed scans were taken on multiple anatase crystal facets, although the [101] orientation (2θ=25.281°) was the only one that consistently provided intensity strong enough for analysis. Quantification of anatase/rutile composition was not done as rutile components were negligible. The software program JADE from Materials Data Inc. and additional software from PANalytical Corp. was used for determination of crystal phase, crystallite sizes, density, and thickness. Average crystallite size was calculated by JADE using peak width and Scherrer's equation. Associated error bars stem from noise in the curve fit and not from a crystallite size distribution. Uncertainty in density measurements from PANalytical software is typically up to 2% of determined value and is included as error bars on figures below.

Electrical characterization for determination of carrier concentration, N_d, employed a Si-TiO_2-Al Schottky diode structure and procedure described elsewhere[30]. In all cases the material was n-type, in accord with previous work[9, 30]. The only procedural difference from that work (intended to save a few fabrication steps) was that corners of the TiO_2 film were abraded with fine sandpaper until bare Si was exposed. With both TiO_2 and Si exposed, contacts were fabricated simultaneously via photolithographic patterning. At the ends of certain ranges tested, samples sometimes experienced electrical conductivity issues. Specimens at 400 °C apparently did not fuse properly, giving the film itself poor conductivity. Some specimens at 650 °C displayed a diffraction peak corresponding to a silicon titanium oxide, which probably created an insulating barrier between the film and substrate.

[‡] Anatase: 00-021-1272, Rutile: 00-021-1276

Results

Density ρ, crystallite size D, and N_d were determined for all sample sets. Films of constant thickness were used to test the effects of growth rate and deposition temperature. Films of varied thickness were used to test the effects of annealing ramp rate and temperature. For convenience, a summary of experimental conditions and major trends is provided in Table 1.

Effect Tested	Thickness (nm)	Growth Rate (nm/cycle)	Deposition Temperature (°C)	Annealing Ramp Rate (°C/min)	Annealing Temperature (°C)	Noteworthy Variations
Growth Rate	100	**0.3 – 7.7**	200	20	550	ρ ↓ 10%, N_d ↓ 2X
Deposition Temperature	100	1.5	**150 - 275**	20	550	$D$$ ↑ 15%, ρ ↑15, N_d ↓ 25%
Annealing Ramp Rate	50 - 325	2.5	200	**1 - 1000**	550	D ↑ ~50%, ρ ↑ 15%
Annealing Temperature	50 - 325	2.25	200	20	**400 - 650**	D ↑ 2X, then ↓ 2X

Table 1: Summary of experimental conditions.

A. Effects of growth rate

Amorphous films were grown at 200 °C to thicknesses of 105 ± 5 nm at rates between 0.25 and 7.5 nm/cycle. Figure 1 shows the resulting variations average crystallite size (as determined from XRD anatase [101] peak). A least-squares fit of the data shows a slight increase in size from 32 to 34 nm in the range 0.25 – 4 nm/cycle, but that increase is within the uncertainty of the fitted line's slope (0.69 ± 1 cycle). Thus, the data are also consistent with no effect of growth rate on crystallite size in this range.

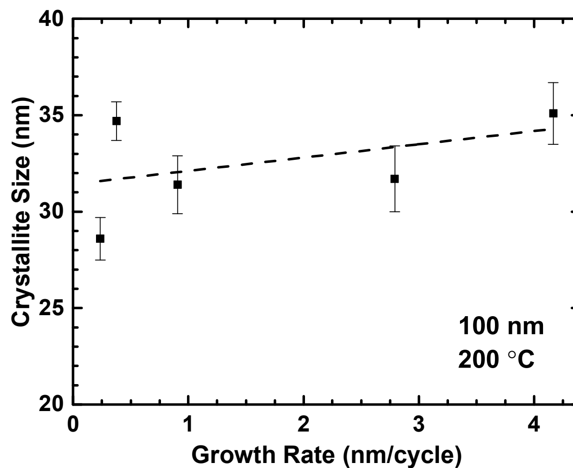

Figure 1: Variation in anatase crystallite size with growth rate. Fitted line is a linear least squares fit.

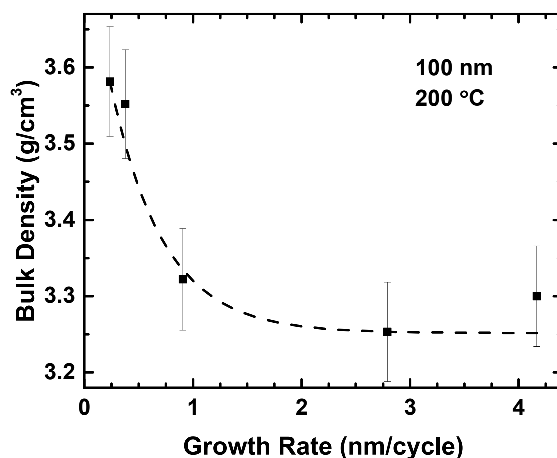

Figure 2: Variation in bulk density with growth rate. Fitted curve is a nonlinear least squares fit of a phenomenological exponential function, serving only to guide the eye.

Figure 2 shows XRR-derived data for bulk density. As is common for ALD-grown films, the density is consistently lower than the single-crystal value for anatase of 3.89 g/cm^3. Significantly, the density decreased with growth rate by about 10% over the range 0.25 – 4 nm/cycle, with most of the change occurring below 1 nm/cycle. Data for 7.5 nm/cycle are not shown because of excessive surface roughness that precluded accurate XRR measurements.

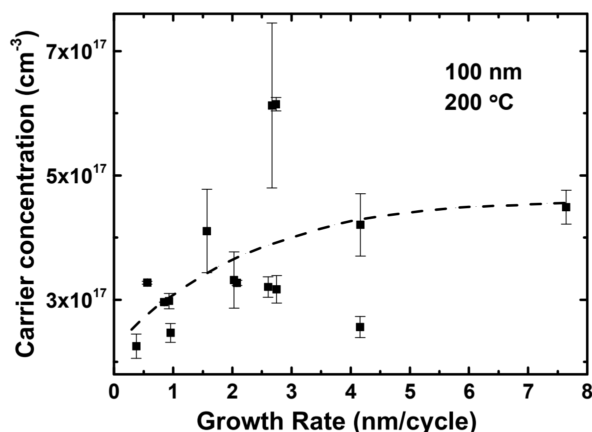

Figure 3: Variation in carrier concentration with growth rate. Added curve is hand drawn, serving only to guide the eye.

Figure 3 shows data for carrier concentration. The absolute magnitudes of a few times 10^{14} cm^{-3} are broadly consistent with values this laboratory has reported previously[6]. Although the data exhibit considerable scatter, carrier concentration increases by roughly a factor of two. The variation of n with growth rate is more gradual than that for density, with the values for N_d leveling off only above roughly 4 nm/cycle.

B. Effects of deposition temperature

To examine the effects of deposition temperature of the amorphous material, films were grown at 1.5 nm/cycle to thicknesses of 100 ± 5 nm at temperatures between 150 and 275 °C. Temperature was restricted at the low end by water vapor reactivity[31] and/or Ti surface mobility[32], and at the high end by a change in TTIP decomposition mechanism[33, 34].

Over this range, Figure 5 shows a noticeable increase in crystallite size by about 15% from about 27 to 32 nm. The variation is approximately linear.

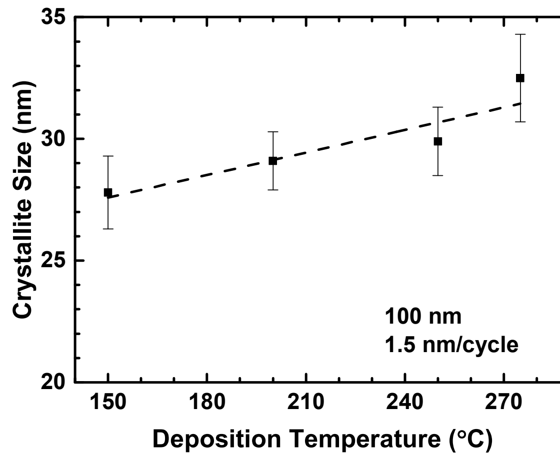

Figure 4: Variation in anatase [101] crystallite size with deposition temperature. Fitted line is a linear least squares fit as a guide to the eye.

Figure 4 shows the resulting changes in bulk density, with the density increasing also increasing approximately linearly by roughly 15% from 3.3 to 3.8 g/cm^3. The latter number lies near the bulk value of 3.89 g/cm^3.

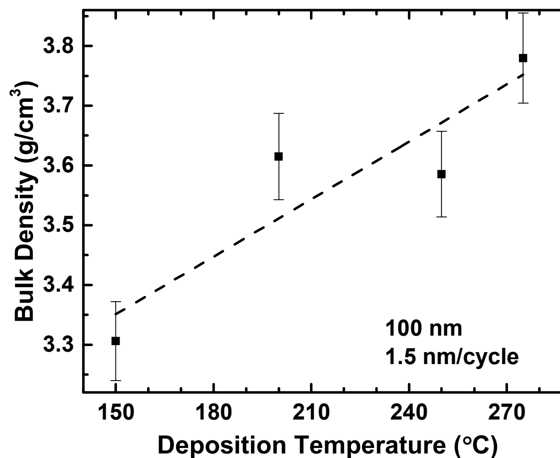

Figure 5: Variation in bulk density with deposition temperature. Fitted line is a linear least-squares fit as a guide to the eye.

Figure 6 shows carrier concentration. The values of N_d are rather noisy, but they decrease with deposition temperature by about 25%.

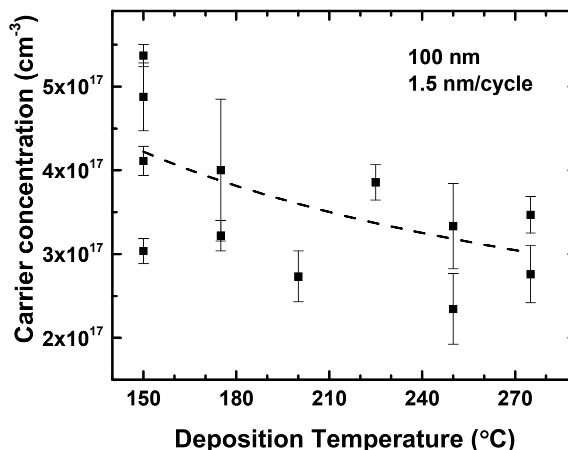

Figure 6: Variation in carrier concentration with synthesis temperature. Fitted curve is a nonlinear least squares fit of a phenomenological power law function, serving only to guide the eye.

C. Effects of annealing ramp rate

To examine the effects of ramp rate up to the steady annealing temperature of 550°C that converts amorphous material to anatase, films were grown at 200°C and 2.5 nm/cycle to thicknesses between 50 and 350 nm at ramp rates ranging from 1 to 1000°C/min.

For crystallite size, thicknesses of only 100 and 300 nm were examined in Figure 7. Here, both the [101] and [200] orientations offered sufficient resolution to provide useful data. Although the two orientations yielded slightly different values for size, these differences exhibited no systematic pattern. There was a steady, linear increase of 50-60% as the logarithm of the ramp rate rose.

Figure 8 shows that bulk density also increased with ramp rate, but did so with a different functional form. Most of the 15% change occurred between 1 and 5°C/min, but the density continued to increase over the entire investigated range. The density at 1°C/min fell between 3.0 and 3.1 g/cm^3 – the lowest values of any observed in this work.

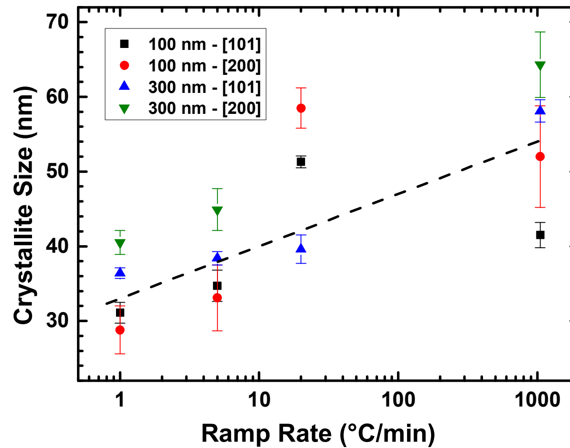

Figure 7: Variation in crystallite size with annealing ramp rate for [101] and [200] crystal faces. Data for 100 nm thickness at 20 °C/min had a slightly altered growth rate of 2.8 nm/cycle. Fitted line is a phenomenological linear least squares fit, serving only to guide the eye.

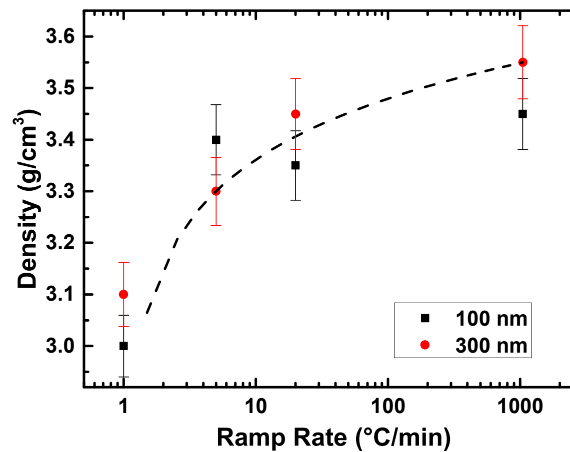

Figure 8: Variation in bulk density with annealing ramp rate. Data for 100 nm thickness at 20 °C/min had a slightly altered growth rate of 2.8 nm/cycle. Fitted curve is a nonlinear least squares fit of a phenomenological logarithmic function, serving only to guide the eye.

Figure 9 shows carrier concentration data plotted vs. film thickness for the entire range of heating rates examined. The values of N_d replicate the decreasing trend as a function of thickness that has been reported previously[9, 30]. However, heating rate exerts no discernible effect.

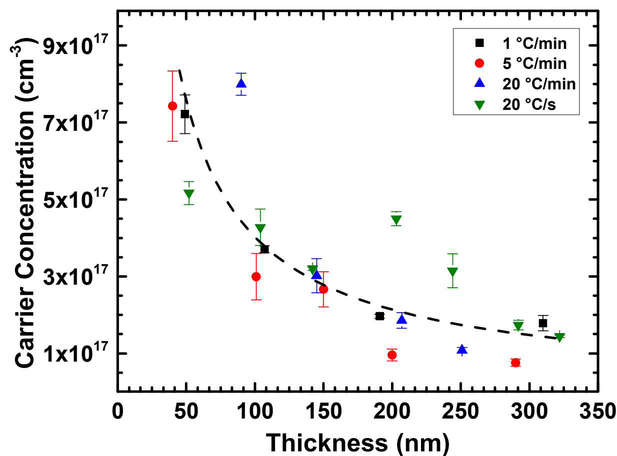

Figure 9: Variation in carrier concentration with annealing ramp rate. Fitted curve is a nonlinear least squares fit of a phenomenological power law function, serving only to guide the eye.

D. Effects of annealing temperature

To examine the effects of steady annealing temperature that converts amorphous material to anatase, films were grown at 200 °C and 2.25 nm/cycle to thicknesses of 80 or 250 nm. Ramp-up was done at 20 °C/min to temperatures between 400 and 650 °C.

Figure 10 shows a sharp increase by a factor of two in crystallite size as the annealing temperature rises from 400 to 450°C. However, the size decreases gradually for further temperature increases back to approximately the original value.

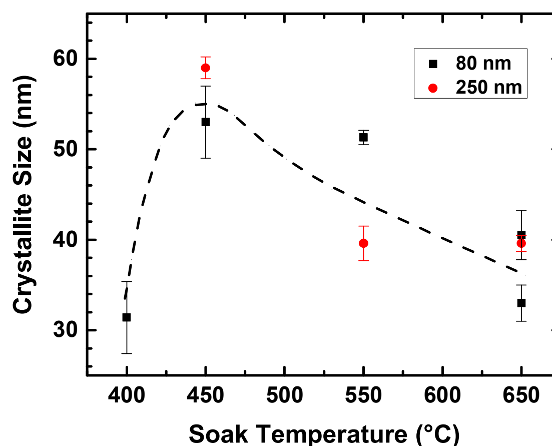

Figure 10: Variation in anatase [101] crystallite size with annealing temperature. Error bars taken from JADE peak fitting results. Added curve is hand drawn, serving only to guide the eye.

Figure 11 shows no perceptible change in bulk density over the range of annealing temperatures tested. Figure 11 shows significant sample to sample scatter in the data.

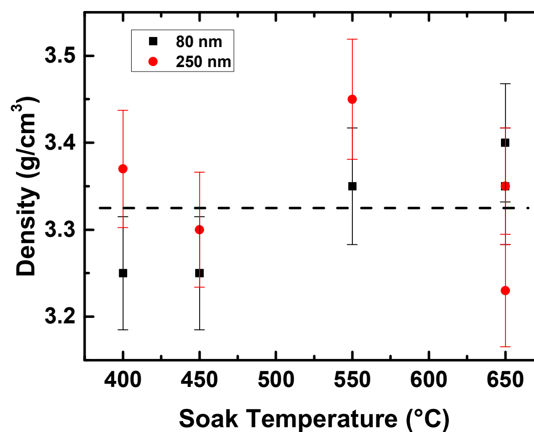

Figure 11: Variation in bulk density with annealing temperature. Added line is a flat guide to the eye.

Figure 12 compares the thickness variation of the carrier concentration for the two annealing temperatures – a format analogous to that of Figure 9. The data for 550°C hint at a slightly stronger thickness variation than for 450°C. However, given the substantial scatter that is evident in Figure 12 and Figure 9, we believe the results in Figure 12 do not provide an adequate basis for conclusively distinguishing a difference between the two annealing temperatures. Accordingly, a single line has been employed to correlate the data phenomenologically.

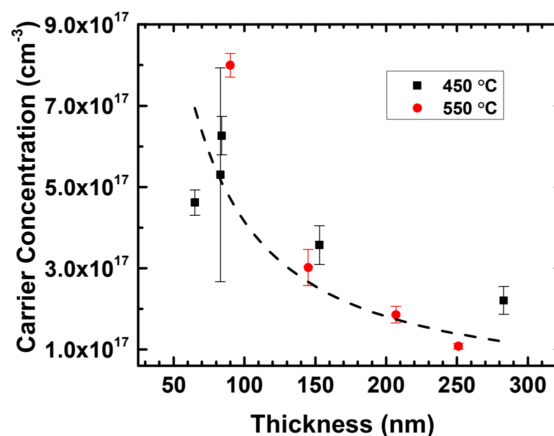

Figure 12: Variation in carrier concentration with thickness for two different annealing temperatures. Data for 550 °C taken from the annealing ramp rate experiment in Fig. 9. Fitted line is a power law fit of the combined data set.

Discussion

The results show that variations in the temperature for depositing the amorphous films propagate into changes in carrier concentration of the final crystalline films as well as their crystallite size and bulk density. Growth rate affects both N_d and density. The ramp rate during post-growth annealing to anatase affects both density and crystallite size, while final annealing temperature affects only crystallite size. These phenomena are complicated. However, they indicate that, even though the as-deposited films are amorphous by standard X-ray diffraction techniques, the films retain a memory of the deposition conditions. This memory is presumably embodied in some type of special ordering that is invisible to X-ray diffraction.

Such ordering has indeed been observed in amorphous Si[24] and TiO_2[25], and computational evidence exists for metal oxides in general[26]. Termed "medium range order," this phenomenon represents a special type of atomic configuration within amorphous semiconductors wherein the atoms are arranged into topologically crystalline grains, roughly 1 nm in diameter, that are isolated and severely strained and therefore do not produce coherent diffraction or sharp Raman peaks. Such grains can be conceptualized as subcritical nuclei for the subsequent growth of crystallites upon annealing.

Early work to identify MRO in amorphous Si relied upon crystal growth kinetics[35, 36] and high resolution electron micrographs[37]. More recently, direct detection in metal oxides has relied upon neutron scattering[38] and fluctuation electron microscopy[39-41]. Efforts to manipulate the MRO for specific purposes have focused on increasing the concentration of ordered regions[28, 29] and use for photoassisted self-assembly[25]. However, little systematic work has been done to link the behavior of MRO to typical material synthesis parameters connected with growth and annealing. The following paragraphs attempt to forge such links where possible.

A. Growth Rate

Although growth rate of the amorphous material exerts little to no effect on crystallite size, the increase in N_d by a factor of two and the decrease in bulk density by 10% are more

noticeable as the growth rate rises. As discussed elsewhere[9], crystallite size as measured by diffraction represents a distinct quantity from grain size without correlation.

It is likely that the amorphous film's "memory" of the growth rate results from the presence of MRO. At slower growth rates, depositing atoms have more time to diffuse on the surface and begin to order themselves in a close prelude to crystal formation. An increasing prevalence of such ordering corresponds to an increasing concentration of MRO regions, which in turn would boost the concentration of crystal nuclei during annealing. More crystallites may lead to an increased concentration of grains that in turn may aid compaction.

We cannot establish these causal links definitively, as the experimental techniques employed here do not measure the concentrations of either crystallites or grains – only crystallite size and average material density. Neither quantity connects definitively to the desired concentrations. Nevertheless, the pronounced changes in density occurring below 1 nm/cycle (*i.e.*, in the vicinity of one monolayer/cycle) support the notion that extended time for surface diffusion aids the formation of MRO. Multiple monolayers deposited in a single cycle would substantially decrease this diffusion time and propagate into less compaction and lower density.

It is notable that N_d and density change in opposite directions in response to growth rate. This trend accords with that observed in response to variations in annealing time[9] as well as growth temperature (described below). By contrast, N_d and density vary in the same direction in response to changes in initial film thickness[9]. This covariance of N_d and density as a function of thickness was not readily explained in Ref [9]. Furthermore, the annealing ramp rate (described below) affects the density significantly but leaves N_d fixed. In general, there is no clear relationship between density and N_d as various synthesis parameters change.

Grain boundaries serve as unintentional donor defects by annihilating or trapping charge carriers[42]. It is energetically favorable for native donor defects such as oxygen vacancies and titanium interstitials to aggregate at grain boundaries[43], although it is less clear whether the interior surfaces of voids serve the same function. By contrast, density depends upon internal void volume and the average atomic packing within the contiguous solid. The lack of consistent

connection between N_d and density therefore suggests that few electrically active defects reside at the interior surfaces of voids; such defects evidently reside principally at the solid-solid interfaces of grain boundaries.

Further deconvolution of the effects of growth rate and the other synthesis variables examined in this work is difficult, however. Thermal annealing of amorphous TiO_2 prompts crystallization that normally originates from either the TiO_2-substrate interface or the TiO_2 free surface. For both interface- and surface-nucleated grain clusters, outward and inward growth propels the voids in the direction of the crystallization front; some ultimately remain trapped within the film. For example, annealing of 200 nm TiO_2 on SiO_2 prepared by sol-gel processing results in the formation of microscopic voids ahead of the growth front within the film[44]. Annealing prompts a reduction in void volume that partly accounts for the densification process. More importantly for the present work, the accumulation of voids near the center of the film implies that spatial variations exist in initial void volume.

Therefore, in addition to whatever MRO-connected kinetics influence the crystallization, there also exists a set of embedded atomic diffusion processes arising from spatial variations in density and perhaps other film properties. The transport issues will be most evident in film thickness studies akin to those of Ref. [9]. Most characterization tools, including those employed here and in Ref. [9], average over the entire film. Thus, disaggregation of kinetic and diffusional processes for atomic transport is difficult and cannot be accomplished in the present work.

B. Deposition Temperature

Increasing the growth temperature of the amorphous material boosts the crystallite size by about 15%. A corresponding decline in N_d by 25%, together with an increase in density by 15%, are also significant. As in the case of deposition rate, N_d and density change in opposite directions. Thus, the MRO-creating enhancements in surface mobility due to increased temperature rationalize the density relationships as in the case of growth rate. The specific

growth rate chosen for the temperature study was 1.5 nm/cycle, which is slightly above the point in Figure 2 where the density levels off. The purpose of this choice was to ascertain whether increasing temperature could compensate for the slight burial of the first-depositing atoms during each cycle of growth. The fact that subsequent annealing yielded high densities up to 3.8 g/cm^3 (near the fully-compact value for anatase) suggests the answer is affirmative.

The increase in crystallite size is more difficult to explain conclusively in terms of MRO. Based upon XRD and ellipsometry data, we assume that crystallite formation and growth occur exclusively during the ramping and annealing steps. Perhaps the increased MRO production with temperature produces more ready-to-grow subcritical nuclei resulting in fewer, larger crystallites. Connection between crystallite size and N_d or density is also difficult to make, as the latter quantity is affected primarily by grain formation. The trends likely demonstrate the same compaction scheme seen with varied growth rate.

C. Annealing Ramp Rate

Increasing the ramp rate used to reach the final annealing temperature boosts both the crystallite size and the bulk density substantially. However, there is no discernible effect on N_d. Clearly the ramp rate affects either the creation of growing crystallites, from either MRO regions or other random nucleation sites available to the film. For simple elementary kinetic steps operating in parallel, higher ramp rates tend to favor steps with large pre-exponential factors[45]. Nucleation is not a simple elementary step, as exemplified by the induction time exhibited by surface nucleation of grains on amorphous TiO_2[25]. Surface crystallization induction times for TiO_2 have been reported in Temperature Programmed XRD experiments, with time scales on the order of minutes[46]. However, if such an induction phenomenon generalizes to nucleation within the bulk, faster ramping may select for only those nucleation sites that are most predisposed to grow. Such selection would reduce the number of growing crystallites (favoring existing MRO), and permit them to ripen to larger sizes leaving fewer chances for crystallites to form grain

boundaries. The resulting smaller number of growing grains may aid compaction and thereby increase bulk density as seen in Figure 8.

D. Annealing Temperature

Increasing the final annealing temperature exerts no clear effect on density or N_d, but induces large and non-monotonic variations in crystallite size. Evidently any time or temperature dependence of the donor concentration for the polycrystalline material originates on a time scale less than the 24 annealing time used here, and the experimental range of temperatures. We have no compelling explanation for the complicated behavior of crystallite size. We comment only that competing kinetic and perhaps diffusional processes are probably at work, either during the latter stages of the ramp phase (whose length depends upon the final temperature) or early in the constant-temperature phase.

Conclusion

Variations in the deposition temperature, growth rate, annealing ramp rate and annealing temperature were employed to determine the effects of synthesis conditions on polycrystalline anatase TiO_2 thin films. Product films were analyzed for final carrier concentration, crystallite size and bulk density with an interest in tying morphological variation to electronic structure. In the cases of deposition conditions, a clear propagation was seen between the changes in synthesis conditions, crystalline film morphology, and final carrier concentration. In the cases of annealing conditions, morphological and electronic trends were found to be independent. Many of these surprising findings can be interpreted in terms of the existence of medium range order in the initial amorphous films, and demonstrate that the MRO can be manipulated to some degree. In the present case, the manipulation was motivated by the desire to control carrier concentration, but other applications may seek to control crystallite size, bulk density, or other material properties not measured here. Although methods for exploiting MRO in amorphous

semiconductors for useful purposes remain in their infancy, the present work points to a richness of behavior that merits closer attention in the future.

Acknowledgements

This work was partially supported by the National Science Foundation (DMR 10-05720 and DMR 13-06822) as well as the Strategic Research Initiatives Program in the College of Engineering at the University of Illinois. X-Ray characterization was performed at the Center for Microanalysis of Materials at the Frederick Seitz Materials Research Laboratory University of the Illinois at Urbana-Champaign. D.E.B. gratefully acknowledges fellowship support from the Dow Chemical Company. We are grateful to Mauro Sardela for assistance in interpretation of X-Ray results, and Dane Sievers for assistance in interpreting *C-V* data and many other insights.

References

1. Haidry AA, Schlosser P, Durina P, et al. Hydrogen gas sensors based on nanocrystalline TiO_2 thin films. *Central European Journal of Physics.* 2011;9(5):1351-1356.
2. Fujishima A, Hashimoto K, Watanabe T. *TiO_2 Photocatalysis: Fundamentals and Applications*: Bkc; 1999.
3. Paz Y, Luo Z, Rabenberg L, Heller A. Photooxidative self-cleaning transparent titanium dioxide films on glass. *Journal of Materials Research.* 1995;10(11):2842-2848.
4. Chung C-J, Lin H-I, Tsou H-K, Shi Z-Y, He J-L. An antimicrobial TiO_2 coating for reducing hospital-acquired infection. *Journal of Biomedical Materials Research Part B: Applied Biomaterials.* 2008;85B(1):220-224.
5. Yan W, Lin-lin W, Ming-yan L. Antifouling and enhancing pool boiling by TiO_2 coating surface in nanometer scale thickness. *AIChE Journal.* 2007;53(12):3062-3076.
6. Takahashi M, Tsukigi K, Uchino T, Yoko T. Enhanced photocurrent in thin film TiO_2 electrodes prepared by sol-gel method. *Thin Solid Films.* 2001;388(1-2):231-236.
7. Zhang Z, Yates JT. Band Bending in Semiconductors: Chemical and Physical Consequences at Surfaces and Interfaces. *Chemical Reviews.* 2014/06/25 2012;112(10):5520-5551.
8. Kapinus EI, Viktorova TI. Kinetics of the photocatalytic degradation of methylene blue on titanium dioxide. *Theoretical and Experimental Chemistry.* 2010;46(3):163-167.
9. Sellers MCK, Seebauer EG. Manipulation of polycrystalline TiO_2 carrier concentration via electrically active native defects. *Journal of Vacuum Science & Technology A.* 2011;29.
10. Seebauer EG, Kratzer MC. Charged point defects in semiconductors. *Materials Science and Engineering: R: Reports.* 2006;55(3-6):57-149.
11. Seebauer EG, Kratzer MC. *Charged Semiconductor Defects: Structure, Thermodynamics and Diffusion*. London: Springer; 2009.
12. Seebauer EG, Noh KW. Trends in semiconductor defect engineering at the nanoscale. *Materials Science and Engineering: R: Reports.* 2010;70(3-6):151-168.
13. Nowotny MK, Sheppard LR, Bak T, Nowotny J. Defect Chemistry of Titanium Dioxide. Application of Defect Engineering in Processing of TiO2-Based Photocatalysts. *The Journal of Physical Chemistry C.* 2014/10/14 2008;112(14):5275-5300.
14. Pärna R, Joost U, Nõmmiste E, et al. Effect of cobalt doping and annealing on properties of titania thin films prepared by sol-gel process. *Applied Surface Science.* 2011;257(15):6897-6907.
15. Xu H, Zhang L. Controllable One-Pot Synthesis and Enhanced Visible Light Photocatalytic Activity of Tunable C-Cl-Codoped TiO_2 Nanocrystals with High Surface Area. *The Journal of Physical Chemistry C.* 2014/09/24 2009;114(2):940-946.
16. Sellers MCK, Seebauer EG. Structural and magnetic properties of Mn-doped anatase TiO_2 films synthesized by atomic layer deposition. *Applied Physics A.* 2011;104(2):583-586.
17. van de Krol R, Goossens A, Schoonman J. Mott-Schottky Analysis of Nanometer-Scale Thin-Film Anatase TiO_2. *Journal of The Electrochemical Society.* May 1, 1997 1997;144(5):1723-1727.
18. Ong SWD. *DESIGN OF BAND-ENGINEERED PHOTOCATALYSTS USING TITANIUM DIOXIDE*. Urbana: Chemical and Biomolecular Engineering, University of Illinois; 2013.

19. Chua YPG, Gunasooriya GTKK, Saeys M, Seebauer EG. Controlling the CO oxidation rate over Pt/TiO_2 catalysts by defect engineering of the TiO_2 support. *Journal of Catalysis.* 2014;311:306-313.

20. Cheng H-E, Hsu C-M, Chen Y-C. Substrate Materials and Deposition Temperature Dependent Growth Characteristics and Photocatalytic Properties of ALD TiO_2 Films. *Journal of The Electrochemical Society.* 2009;156(8):D275-D278.

21. Wang H, Wang T, Xu PEI. Effects of substrate temperature on the microstructure and photocatalytic reactivity of TiO_2 films. *Journal of Materials Science: Materials in Electronics.* 1998;9(5):327-330.

22. Kim SK, Hoffmann-Eifert S, Reiners M, Waser R. Relation Between Enhancement in Growth and Thickness-Dependent Crystallization in ALD TiO_2 Thin Films. *Journal of The Electrochemical Society.* 2011;158(1):D6-D9.

23. Pore V, Kivela T, Ritala M, Leskela M. Atomic layer deposition of photocatalytic TiO_2 thin films from TiF_4 and H_2O. *Dalton Transactions.* 2008(45):6467-6474.

24. Diehl F, Herbst W, Bauer S, Schröder B, Oechsner H. Creation of metastable defects in a-Si:H by keV-electron irradiation at different temperatures. *Journal of Non-Crystalline Solids.* 1996;198-200, Part 1:436-440.

25. Kondratenko YV, Seebauer EG. Directed self-assembly by photostimulation of an amorphous semiconductor surface. *AIChE.* 2010;56(12):3206-3211.

26. Nishio K, Miyazaki T, Nakamura H. Universal Medium-Range Order of Amorphous Metal Oxides. *Physical Review Letters.* 2013;111(15):155502.

27. Gibson JM, Treacy MMJ, Voyles PM, Jin HC, Abelson JR. Structural disorder induced in hydrogenated amorphous silicon by light soaking. *Applied Physics Letters.* 1998;73(21):3093-3095.

28. Gerbi JE, Voyles PM, Treacy MMJ, Gibson JM, Abelson JR. Increasing medium-range order in amorphous silicon with low-energy ion bombardment. *Applied Physics Letters.* 2003;82(21):3665-3667.

29. Law F, Widenborg PI, Luther J, Hoex B. Medium range order engineering in amorphous silicon thin films for solid phase crystallization. *J. Appl. Phys.* 2013;113(19).

30. Sellers MCK, Seebauer EG. Measurement method for carrier concentration in TiO2 via the Mott-Schottky approach. *Thin Solid Films.* 2011;519(7):2103-2110.

31. Aarik J, Aidla A, Uustare T, Ritala M, Leskel¨a M. Titanium isopropoxide as a precursor for atomic layer deposition: characterization of titanium dioxide growth process. *Applied Surface Science.* 2000;161(3-4):385-395.

32. Sladek KJ, Herron HM. Titanium Dioxide Coatings. Room Temperature Deposition. *Product R&D.* 2013/07/08 1972;11(1):92-96.

33. Rahtu A, Ritala M. Reaction Mechanism Studies on Titanium Isopropoxide–Water Atomic Layer Deposition Process. *Chemical Vapor Deposition.* 2002;8(1):21-28.

34. Fictorie CP, Evans JF, Gladfelter WL. Kinetic and mechanistic study of the chemical vapor deposition of titanium dioxide thin films using tetrakis-(isopropoxo)-titanium(IV). *Journal of Vacuum Science & Technology A.* 1994;12(4):1108-1113.

35. Llera-Hurlburt D, Dalton AS, Seebauer EG. Temperature-dependent surface diffusion parameters on amorphous materials. *Surface Science.* 2002;504:244-252.

36. Sakai A, Tatsumi T, Ishida K. Growth kinetics of Si hemispherical grains on clean amorphous-Si surfaces. *Journal of Vacuum Science & Technology A.* 1993;11(6):2950-2953.

37. Krivanek OL, Gaskell PH, Howie A. Seeing order in 'amorphous' materials. *Nature.* 1976;262(5568):454-457.

38. Pickup DM, Sowrey FE, Drake KO, Smith ME, Newport RJ. New insights into medium-range order around titanium in sol-gel derived silica through isotope difference neutron diffraction and reverse Monte Carlo modelling. *Chemical Physics Letters.* 2004;392:503-507.

39. Voyles PM, Gibson JM, Treacy MMJ. Fluctuation microscopy: a probe of atomic correlations in disordered materials. *Journal of Electron Microscopy.* 2000;49(2):259-266.

40. Lee B-S, Burr GW, Shelby RM, et al. Observation of the Role of Subcritical Nuclei in Crystallization of a Glassy Solid. *Science.* 2009;326(5955):980-984.

41. Lee B-S, Bishop SG, Abelson JR. Fluctuation Transmission Electron Microscopy: Detecting Nanoscale Order in Disordered Structures. *ChemPhysChem.* 2010;11(11):2311-2317.

42. Lu H, Schaff WJ, Eastman LF, et al. Growth of a-plane InN on r-plane sapphire with a GaN buffer by molecular-beam epitaxy. *Applied Physics Letters.* 2003;83(6):1136-1138.

43. Nowotny J, Bak T, Burg T, Nowotny MK, Sheppard LR. Effect of Grain Boundaries on Semiconducting Properties of TiO_2 at Elevated Temperatures. *The Journal of Physical Chemistry C.* 2014/11/28 2007;111(27):9769-9778.

44. Exarhos GJ, Aloi M. Crystallite growth kinetics in isothermally annealed sol-gel films. *Thin Solid Films.* 1990;193-194, Part 1:42-50.

45. Hall RB, DeSantolo AM. Pulsed laser induced excitation of metal surfaces: Application as a probe of surface reaction kinetics of methanol on Ni. *Surface Science.* 1984;137(2-3):421-441.

46. Kirsch BL, Richman EK, Riley AE, Tolbert SH. In-Situ X-ray Diffraction Study of the Crystallization Kinetics of Mesoporous Titania Films. *The Journal of Physical Chemistry B.* 2014/12/08 2004;108(34):12698-12706.